Fabrication of CoFe/C@polypyrrole composites with efficient electromagnetic wave absorption properties

Qu Lin[1,2,3], Wang Yajing[1,2,3], Yuan Wenpei[1,2,3], Liu Pengyu[1,2,3],
Zhang Yanlan[1,2,3,*], Wang Yongzhen[1,2,3,*]

(1. *College of Materials Science and Engineering*, *Taiyuan University of Technology*, *Taiyuan* 030024, *China*;
2. *Innovation Research Center for Materials Genetic Engineering*, *Taiyuan University of Technology*, *Taiyuan* 030024, *China*;
3. *Shanxi Joint Laboratory of Coal Based Solid Waste Resource Utilization and Green Ecological Development*, *Taiyuan* 030024, *China*)

Abstract: Recently, increasingly severe electromagnetic radiation has caused harm to precision equipment and human health, which requires the development of effective electromagnetic wave (EMW) absorption materials. These materials require both a strong absorption and a broad bandwidth at low filling rates and small thicknesses. To meet this requirement we have constructed a cobalt-iron/carbon@polypyrrole (CoFe/C@PPy) composite by a two-step synthesis process. The first is the fabrication of magnetic CoFe/C fibers, followed by their coating with a PPy layer with a controlled thickness. This combination of materials results in a magnetic loss from CoFe/C and a dielectric loss from PPy which improves both impedance matching and EMW dissipation. An optimized material has a PPy layer with a thickness of 2.0 mm and a loading of 10% and has a minimum reflection loss ($RL_{\min}$) of −45.6 dB at 14.64 GHz, and the corresponding effective absorption bandwidth is 5.12 GHz. Furthermore, CST Studio simulations and far-field radar cross-section (RCS) analysis validate its practical use, showing a notable RCS reduction of up to 37.5 dBm^2 for a perfect electric conductor.

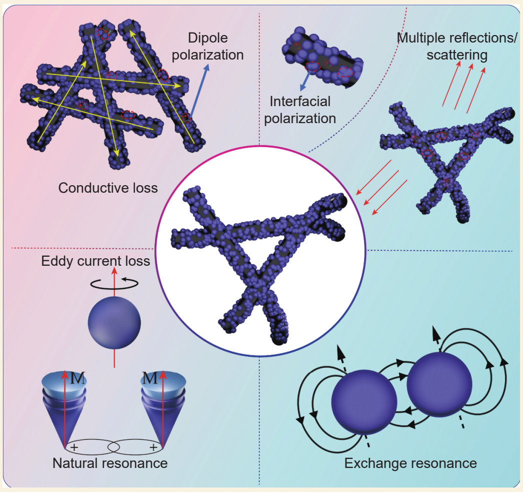

Key words: Electromagnetic wave absorption；Conductive loss；Interface polarization；CoFe alloy；Structural design

1 Introduction

With the advancement of wireless technology, the application of electromagnetic wave (EMW) technology has considerably expanded in the military and civilian sectors, remarkably enhancing the quality of human life[1–6]. However, this progress has caused severe EMW pollution, which has emerged alongside water, air, and soil pollution. Severe electromagnetic radiation disrupts the operation of precision equipment and poses health risks to humans[7–9]. The escalating severity of electromagnetic radiation urges the development of thin, light, broadband and strong wave-absorbing materials.

Based on material compositions, widely studied wave-absorbing materials primarily include ferrite-based materials (such as nickel–zinc ferrite[10] and high-entropy spinel ferrite[11]), carbon-based materials (including graphene[12], carbon nanotubes[13] and carbon nanofibers[14]), ceramic-based materials (for example, silicon carbide[15]), and polymer-based materials (for example, polypyrrole [PPy][16]). Among them, recently, carbon-based materials have gained widespread attention because of their low density, excellent corrosion resistance, high conductivity, wide availability, low cost and high chemical stability[17]. However, single-component carbon materials often exhibit poor impedance matching, limiting their ap-

Received: November 17, 2025
Revised: January 12, 2026
Accepted: January 12, 2026

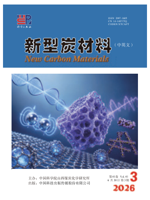

plications. Magnetic metals such as iron (Fe)[18], cobalt (Co)[19] and nickel (Ni)[20], along with their alloys, exhibit excellent magnetic loss and high saturation magnetization (*M*s). However, single-component magnetic materials often possess high density and poor stability. Therefore, incorporating magnetic components into carbon materials is an effective strategy for enhancing wave absorption performance. For instance, Guo et al. prepared a Ni@C/porous carbon composite that achieved a minimum reflection loss ($RL_{\min}$) of −37.6 dB at a thickness of 1.9 mm and an effective absorption bandwidth (*EAB*) of 7.52 GHz at a thickness of 2.0 mm[21]. Similarly, Tang et al. synthesized a Co@C/C-20 composite through acetic acid etching and high-temperature pyrolysis, achieving an $RL_{\min}$ of −49.8 dB and an *EAB* of 5.0 GHz at only 11% (mass fraction) filling rate[22].

Conductive polymers, such as polyphenylene vinylene, polythiophene, polyaniline (PANI) and PPy, have recently garnered considerable attention in wave-absorbing materials. Compared with traditional inorganic materials, conductive polymers possess conjugated π-bond structures that facilitate the formation of extensive electron-transport networks[23]. Among these, PANI and PPy have been the most extensively researched polymers. However, PANI synthesis typically requires acids[24], raising environmental concerns. Consequently, PPy serves as a more environmentally friendly alternative. Numerous studies have demonstrated that incorporating PPy into various materials substantially enhances the wave-absorbing performance. For example, the CuS/Fe_3O_4@PPy composite synthesized by Dai et al. exhibited an $RL_{\min}$ of −74.12 dB at a thickness of 2.96 mm and an *EAB* of 4.6 GHz at the thickness of 1.68 mm[25]. The introduction of PPy improves bonding strength and promotes EMW absorption through multiple refractions within the intercalated structure. In the Ni/NiO/C/MnO_2@PPy composites prepared by Feng et al., PPy introduction markedly enhanced dielectric loss and stability, achieving an $RL_{\min}$ of −56.23 dB at a thickness of 3.87 mm and an *EAB* of 6.86 GHz at a thickness of 1.97 mm[26].

Herein, we successfully synthesized CoFe/C@PPy composites through electrospinning, high-temperature calcination, and oxidative polymerization. A systematic investigation of the EMW absorption properties of the CoFe/C@PPy composites revealed that the PPy content considerably influences overall performance. By controlling the PPy content, the electromagnetic parameters can effectively be regulated, thereby enhancing EMW absorption performance. Integrating multiple components along with a rational structural design endows the composites with outstanding EMW absorption properties. To assess application potential, we simulated the stealth performance of the composite material using computer simulation technology（CST）and conducted radar cross-section (RCS) analysis. This study provides a strong basis for developing lightweight, broadband, and highly effective EMW absorption materials.

2 Experimental

2.1 Chemical reagents

N, N-dimethylformamide (DMF) was obtained from Sinopharm Chemical Reagent Co., Ltd. Iron acetylacetonate ($C_{15}H_{21}FeO_6$), cobalt acetylacetonate ($Co(C_5H_7O_2)_2{\cdot}xH_2O$), and iron chloride ($FeCl_3$) were sourced from Aladdin. Sodium dodecylbenzene sulfonate (SDBS), polyacrylonitrile (PAN, Mw = 150 000), and pyrrole (Py) were procured from Macklin. Ultrapure water was prepared in the laboratory. All reagents were used directly without any further purification.

2.2 Preparation of CoFe/C composite fibers

PAN (1 g) was added to DMF (10 mL) and stirred at 50 °C until completely dissolved. Subsequently, $C_{15}H_{21}FeO_6$ (0.5295 g) and $Co(C_5H_7O_2)_2{\cdot}xH_2O$ (0.3855 g) were added to the solution, and the mixture was stirred at room temperature for 12 h until fully dissolved. The resulting solution was transferred to a 20 mL syringe. Electrospinning parameters were set as follows: 23 G needle, roller speed of 400 r/min, injection pump speed of 0.0005 mm/s, needle-to-collector distance of 8 cm, applied voltage of 15 kV, ambient temperature of 30 °C, and relative humidity of approximately 60%. The product was dried overnight at 60 °C in an oven. Subsequently, carbonization was conducted at 800 °C for 2 h under N_2 atmosphere after preoxidation at 250 °C for 2 h. The carbonized CoFe/C fibers were designated as CFC.

2.3 Preparation of CoFe/C@PPy composites

The introduction of PPy was based on a previous study[27]. A total of 13 mg of SDBS and varying volumes of Py (50, 100 and 150 μL) were dissolved in ultrapure water and ultrasonicated for 10 min. Subsequently, 100 mg of CoFe/C fibers were added and stirred for 2 h to form the solution A. Separately, 0.4 g of $FeCl_3 \cdot 6H_2O$ was dissolved in 5 mL of ultrapure water to form the solution B, which was poured into the solution A and stirred for 2 h. Finally, the resulting mixture was washed several times with ultrapure water and freeze-dried at −40 °C. The CoFe/C@PPy composites with 50, 100 and 150 μL of PPy were designated as CFC-1, CFC-2 and CFC-3, respectively.

2.4 Characterization

Phase analysis of the samples was conducted using X-ray diffraction (XRD, Aeris Malvern Panalytical, UK). Morphology was observed using scanning electron microscopy (SEM, Zeiss Gei-mini360, Germany) and transmission electron microscopy (TEM, FEI Tecnai F20, USA). The hysteresis loop and initial magnetization curve of the samples were measured using a vibrating sample magnetometer (LakeShore-7404, USA). The chemical composition and valence states of CFC-2 were analyzed using X-ray photoelectron spectroscopy (XPS, Thermo Scientific K-Alpha, USA). Structural analysis was performed using Fourier-transform infrared spectroscopy (FTIR, Thermo Fisher Scientific Nicolet iS20, USA). Each sample was uniformly mixed with paraffin with a mass ratio of 1 ∶ 9 and subsequently pressed into a standard toroidal sample with inner and outer diameters of 3.04 and 7.00 mm, respectively. Electromagnetic parameters were obtained using a vector network analyzer (MS46322B, Anritsu, Japan) over 2–18 GHz.

3 Results and discussion

3.1 Physicochemical properties

Fig. 1 illustrates the synthesis route of CoFe/C@PPy composites. Initially, metal-containing PAN-based fibers were prepared by electrospinning. Subsequently, CoFe/C fibers were synthesized through a two-step calcination process. Finally, varying amounts of PPy were loaded onto the CoFe/C fibers by oxidative polymerization.

The morphology and microstructure of the 4 samples were characterized by SEM. As illustrated in Fig. 2a, CFC after high-temperature carbonization exhibits a randomly oriented fiber structure with a mean diameter of approximately 182 nm and a relatively rough surface, providing abundant nucleation and growth sites for PPy. Fig. 2(b–d) display the SEM images of CFC-1, CFC-2 and CFC-3. The images show that increasing the amount of PPy leads to a gradual increase in PPy deposition on the fibers. Fig. 2(e–h) present the TEM images of CFC, revealing a lattice spacing of 0.202 nm corresponding to the (110) plane of the CoFe alloy, thereby confirming the presence of the CoFe alloy. Fig. 2(i–l) presents the EDS elemental mapping of CFC-2, demonstrating the homogeneous distribution of C, N, Co and Fe.

Fig. 3a shows the crystal structures of the CFC, CFC-1, CFC-2 and CFC-3 composites. All XRD patterns of samples exhibit distinct diffraction peaks at 44.9°, 65.3° and 82.7° corresponding to the (110), (200) and (211) planes of the CoFe alloy, respectively (PDF#44-1433)[28], thus confirming the presence of CoFe alloy. For CFC, the broad peak at 25° corresponds to amorphous carbon, whereas for CFC-1, CFC-2 and CFC-3, the broad peaks at 25° are attributed to PPy and amorphous carbon[29]. Fig. 3b presents the FTIR spectra of the 4 samples, with the magnified spectrum of CFC-2 presented in Fig. 3c. The peaks at 1556 and 1453 cm^{-1} are assigned to C═C stretching vibrations of the Py ring[30]. The peaks at 885 and 1047 cm^{-1} correspond to out-of-plane bending and in-plane C—H vibration, respectively[25]. The peaks at 1394, 1186 and 966 cm^{-1} are attributed to in-plane vibration of ═C—H, in-plane deformation of C—C, and stretching vibration of C—N, respectively[29]. Fig. 3d displays the hysteresis loops of the 4 samples, all exhibiting an S-shape, indicating ferromagnetic

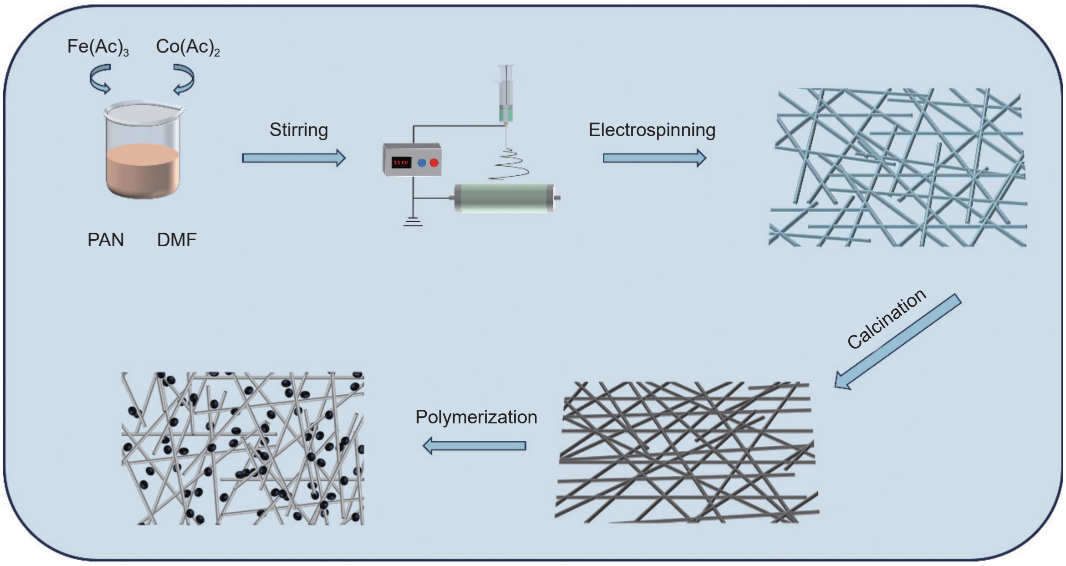

Fig. 1 Schematic of the preparation process of CoFe/C@PPy composites

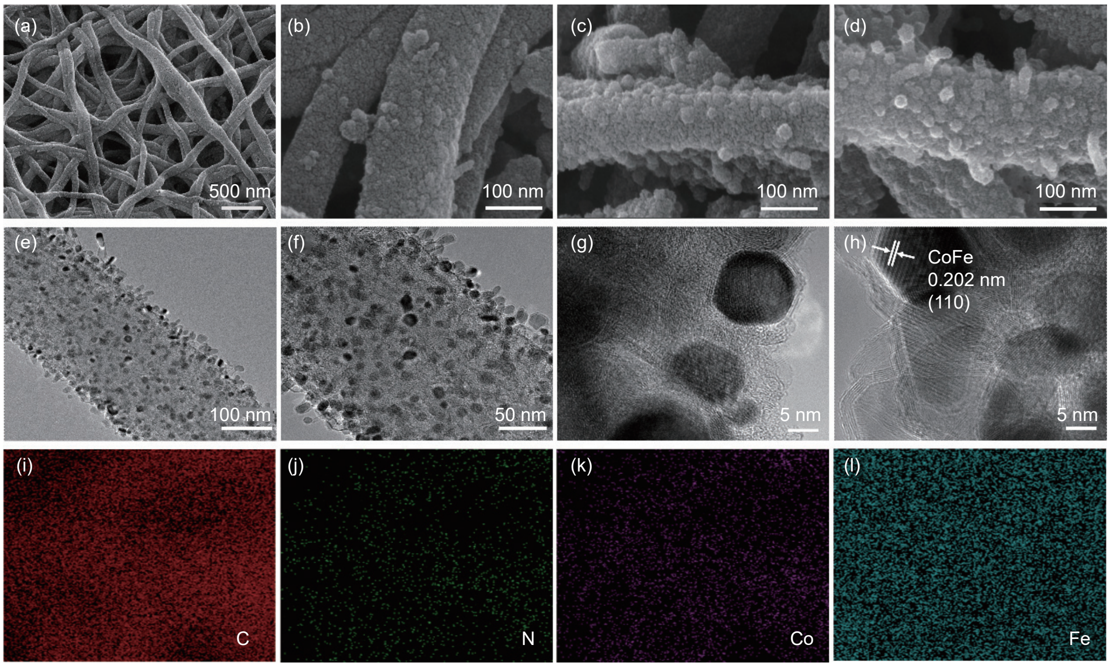

Fig. 2 (a–d) SEM images of CFC, CFC-1, CFC-2 and CFC-3. (e–h) TEM images of CFC. EDS elemental mapping of CFC-2 (i) C, (j) N, (k) Co and (l) Fe

properties. The *M*s values of CFC, CFC-1, CFC-2 and CFC-3 are 39.67, 23.23, 21.81 and 19.36 emu/g, respectively. The progressive decrease in *M*s with increasing the PPy content is primarily attributed to the increased mass stemming from the incorporation of nonmagnetic PPy. The coercivity (*H*c) values of CFC, CFC-1, CFC-2 and CFC-3 are 379.60, 399.24, 416.38 and 407.19 Oe, respectively. The increase in *H*c after PPy addition may result from enhanced magnetic anisotropy owing to interfacial charge transfer involving PPy[31].

The surface composition and chemical valence states of CFC-2 were analyzed using XPS. As shown in Fig. 4a, the XPS survey spectrum reveals the presence of Co, Fe, C and N elements. The C 1s spectrum (Fig. 4b) is deconvoluted into 3 peaks at 284.4, 285.5 and 287.5 eV, corresponding to C—C/C=C, C=N and C=O, respectively[29,32]. The N 1s spectrum (Fig. 4c) shows peaks at 399.5, 400.2 and 402.0 eV, attributed to pyridinic N, pyrrolic N and graphitic N,

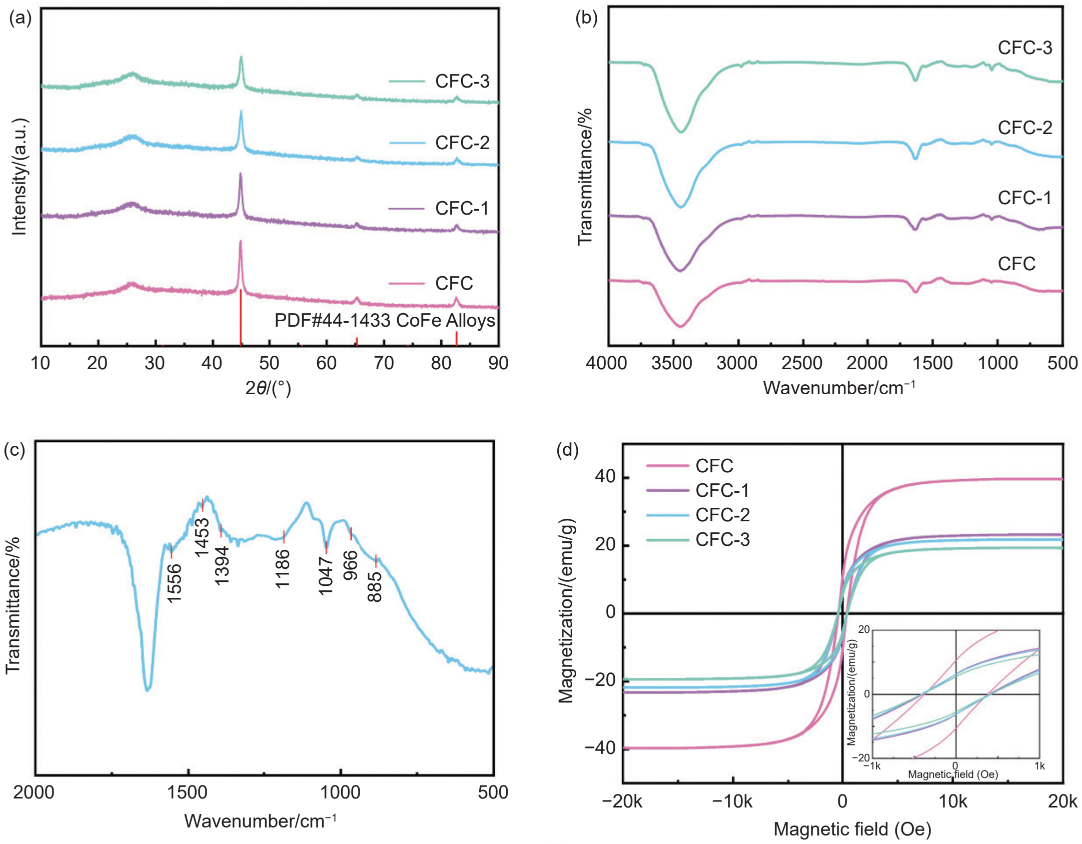

Fig. 3 (a) XRD patterns of CFC, CFC-1, CFC-2, and CFC-3. (b) FTIR spectra of CFC, CFC-1, CFC-2 and CFC-3. (c) Magnified spectrum of CFC-2. (d) Magnetic hysteresis loops of CFC, CFC-1, CFC-2 and CFC-3

respectively[25]. The Co 2p spectrum (Fig. 4d) shows the Co $2p_{1/2}$ peak at 797 eV and the Co $2p_{3/2}$ peak at 781.9 eV, both associated with Co^{2+}. The peaks at 776.5 and 793.7 eV correspond to Co^0, while the peaks at 786.7 and 803.2 eV are attributed to 2 satellite features[31]. The Fe 2p spectrum (Fig. 4e) exhibits a peak at 706 eV, corresponding to Fe^0 of Fe atoms in the CoFe alloy. The peak at 719.4 eV is indicative of the shakeup satellite of Fe^{3+}, and the peaks at 711.9 and 725.1 eV correspond to Fe $2p_{3/2}$ and Fe $2p_{1/2}$, respectively[32].

3.2 EMW absorption

The relative complex permittivity ($\varepsilon_r = \varepsilon' - j\varepsilon''$) and relative complex permeability ($\mu_r = \mu' - j\mu''$) are 2 crucial parameters for evaluating the EMW absorption performance of absorbing materials. The real part of the permittivity (ε') and real part of the permeability (μ') represent the ability to store electromagnetic energy, whereas the imaginary parts (ε'') and (μ'') represent the ability to dissipate electromagnetic energy[33]. The relative complex permittivity ε_r is primarily associated with conduction and polarization losses, with the latter including interfacial, dipole, defect-induced, electronic, ionic and molecular polarizations. However, electronic, ionic and molecular polarizations are not considered here as they typically occur in the high frequency range (10^3–10^6 GHz)[34]. Within 2–18 GHz, the relative complex permeability μ_r is mainly related to natural resonance, exchange resonance, and eddy current loss[35]. Fig. 5(a, b) show the frequency-dependent variation of ε' and ε'' for the four samples. Evidently, all samples exhibit similar trends, characterized by a notable decrease in the low-frequency region before stabilizing. The ε' and ε'' of all samples decrease with increasing frequency, consistent with frequency dispersion phenomena[36]. The ε' and ε'' values for CFC, CFC-1, CFC-2 and CFC-3 increase sequentially. In particular, the values are as follows: CFC (3.4–3.7 and 0.2–0.3), CFC-1 (5.3–7.3 and 1.3–3.1), CFC-2 (6.9–11.2 and 3.0–7.2), and

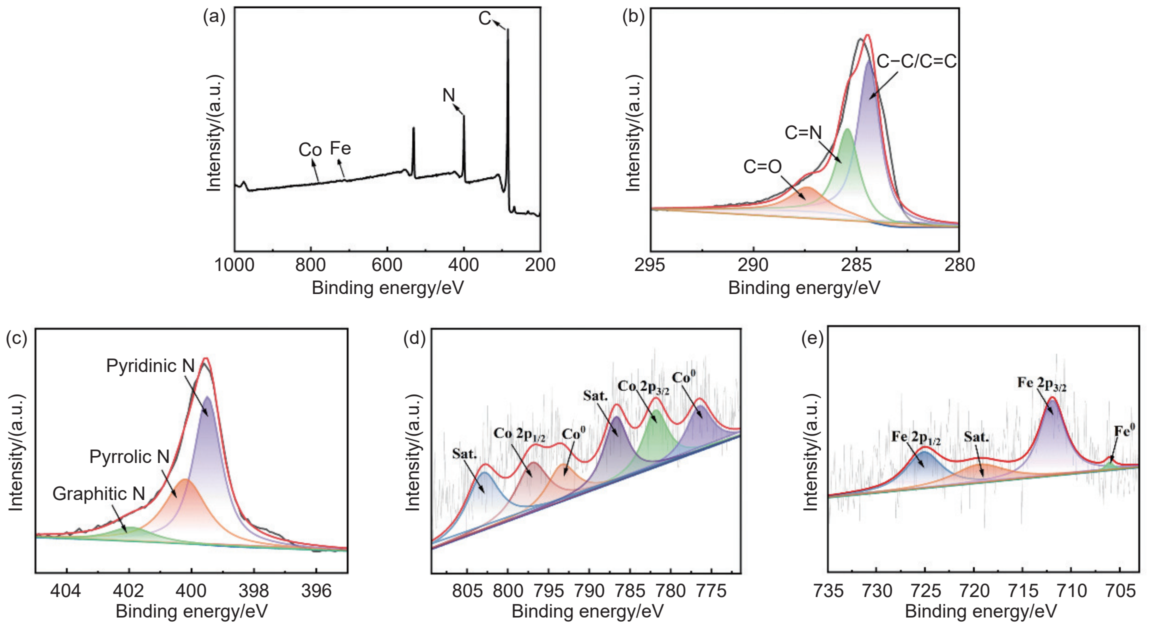

Fig. 4 XPS spectra of (a) CFC-2, and its high resolution spectra of (b) C 1s, (c) N 1s, (d) Co 2p and (e) Fe 2p

CFC-3 (9.6–15.3 and 4.6–13.8). The conductivity of PPy introduces free charges, causing interfacial polarization under an alternating electric field, which increases the ε' and ε'' of the composite materials.

In addition to dielectric loss, magnetic loss substantially impacts the EMW absorption performance of materials. Fig. 5(d, e) show the frequency-dependent variation of μ' and μ'' for the 4 samples. Evidently, the μ' and μ'' of the 4 samples exhibit decreasing trends with increasing frequency. The magnetism of these samples arises from Co–Fe nanoparticles distributed on the fiber surface, contributing to their magnetic properties. Notably, CFC-2 demonstrates the largest μ'', indicating that it possesses the strongest capacity for EMW dissipation. The μ'' values of the 4 samples may yield negative values in certain frequency ranges, possibly due to defects and the high conductivity of the materials. These factors induce notable current

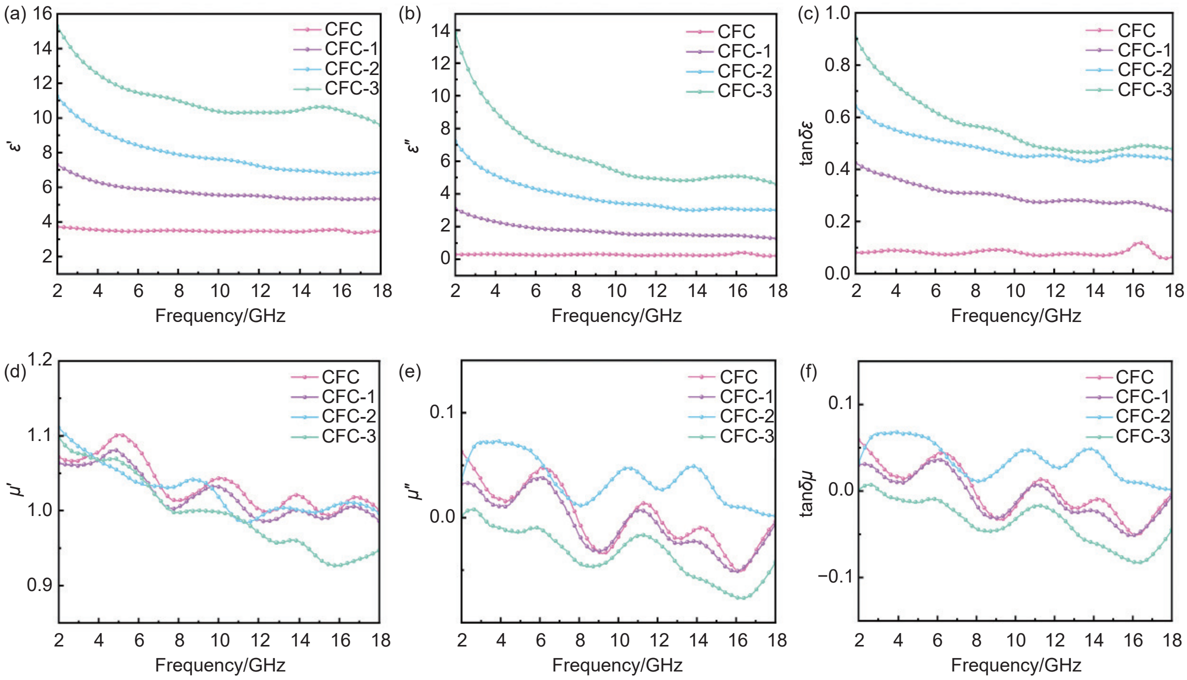

Fig. 5 Electromagnetic parameters of CFC, CFC-1, CFC-2, CFC-3: (a) ε', (b) ε'', (c) $\tan\delta\varepsilon$, (d) μ', (e) μ'', and (f) $\tan\delta\mu$

loops, generating induced currents that produce new induced magnetic fields. When the intensity of the induced magnetic field surpasses that of the original field, negative μ'' values are observed. Moreover, negative μ'' values enhance EMW absorption[37]. The dielectric loss tangent ($\tan\delta\varepsilon = \varepsilon''/\varepsilon'$) and the magnetic loss tangent ($\tan\delta\mu = \mu''/\mu'$) represent the capabilities of dielectric and magnetic loss, respectively[38–39]. Fig. 5(c, f) show the curves of $\tan\delta\varepsilon$ and $\tan\delta\mu$ as the functions of frequency. In Fig. 5c, the $\tan\delta\varepsilon$ of samples containing PPy is considerably higher than that of samples without PPy and $\tan\delta\varepsilon$ increases progressively with the PPy content. This suggests that incorporating PPy enhances material dielectric loss. However, Fig. 5f shows that PPy addition has negligible effects on magnetic loss. The magnetic loss primarily influences EMW absorption performance by adjusting the impedance matching of the material. Furthermore, $\tan\delta\varepsilon$ is substantially larger than $\tan\delta\mu$, indicating that dielectric loss is dominant.

The *RL* of CFC, CFC-1, CFC-2 and CFC-3 was calculated using the transmission line theory and the measured electromagnetic parameters, as described in Eqs. (1–3)[40–41].

$$RL = 20\log_{10}\left|\frac{Z_{\mathrm{in}}-Z_0}{Z_{\mathrm{in}}+Z_0}\right| \tag{1}$$

$$Z_{\mathrm{in}} = Z_0\sqrt{\frac{\mu_{\mathrm{r}}}{\varepsilon_{\mathrm{r}}}}\tan h\left(j\frac{2\pi f d\sqrt{\mu_{\mathrm{r}}\varepsilon_{\mathrm{r}}}}{c}\right) \tag{2}$$

$$Z_0 = \sqrt{\frac{\mu_0}{\varepsilon_0}} \tag{3}$$

where ε_0 and μ_0 represent the vacuum permittivity and permeability, respectively, Z_{in} denotes the input impedance of the material, Z_0 signifies free-space impedance, f indicates EMW frequency, d represents the material thickness and c is the speed of light.

Fig. 6 presents the 2D and 3D *RL* representations and corresponding top views for CFC, CFC-1, CFC-2 and CFC-3 at a filling rate of 10%. For CFC, negligible EMW absorption is observed (Fig. 6(a, e, i)). For CFC-1, the RL_{min} is −14.73 dB at 5.0 mm thickness, with an *EAB* of 1.76 GHz (5.52–7.28 GHz) (Fig. 6(b, f, j)). CFC-2 shows an RL_{min} of −45.6 dB at 14.64 GHz with a 2.0 mm thickness, with an *EAB* of 5.12 GHz (12.48–17.6 GHz) (Fig. 6(c, g, k)). CFC-3 achieves an RL_{min} of −28.03 dB at 14.16 GHz at a thickness of only 1.7 mm, with an EAB of 3.92 GHz (12.56–16.48 GHz) (Fig. 6(d, h, l)). Evidently, CFC-2 demonstrates the lowest *RL* value and the widest *EAB*, whereas CFC-3 achieves the lowest matching thickness. Overall, CFC-2 exhibits the best EMW absorption performance. These results indicate that incorporating PPy onto the fibers markedly enhances EMW absorption, and controlling the PPy content allows effective regulation of the electromagnetic parameters.

Impedance matching refers to the ratio of the material’s impedance to that of free space (Z_{in}/Z_0). Effective impedance matching promotes penetration of EMW into the absorbing material, whereas impedance mismatch causes reflection of incident EMW at the air–material interface. Consequently, in practical applications, impedance matching should be as close to 1 as possible. In this study, a $|\mathit{\Delta}|$ function is introduced to assess the degree of impedance matching, calculated using Eqs. (4–7)[42].

$$\sin h^2(Kfd) = M \tag{4}$$

$$K = \frac{4\pi\sqrt{\mu_{\mathrm{r}}'\varepsilon_{\mathrm{r}}'}}{c}\times\frac{\sin\left(\frac{\delta_\varepsilon+\delta_\mu}{2}\right)}{\cos\delta_\varepsilon\cos\delta_\mu} \tag{5}$$

$$M = \frac{4\mu'\cos\delta_\varepsilon\varepsilon'\cos\delta_\mu}{(\mu'\cos\delta_\varepsilon-\varepsilon'\cos\delta_\mu)^2+\left(\tan\frac{\delta_\mu-\delta_\varepsilon}{2}\right)^2\times(\mu'\cos\delta_\varepsilon+\varepsilon'\cos\delta_\mu)^2} \tag{6}$$

$$|\mathit{\Delta}| = \left|\sin h^2(Kfd)-M\right| \tag{7}$$

where the $|\mathit{\Delta}|$ parameter represents the deviation of the input impedance of the absorbing material from the optimal impedance. Smaller $|\mathit{\Delta}|$ values indicate that the impedance of the absorbing material is closer to that of free space. When $|\mathit{\Delta}|$ equals 0, EMW is essentially not reflected. In general, $|\mathit{\Delta}| <0.4$ is considered sufficient for practical applications. Fig. 7 illustrates the impedance matching $|\mathit{\Delta}|$ for CFC-1, CFC-2 and CFC-3. Introducing PPy considerably improves impedance matching for CFC-1, CFC-2 and CFC-3. For CFC-1, $|\mathit{\Delta}| <0.4$ is observed in the high-frequency region, with a relatively thick matching thickness of 4.0–5.0 mm. By contrast, for CFC-2 and CFC-3, $|\mathit{\Delta}| <0.4$ predominantly occurs at thinner thicknesses, con-

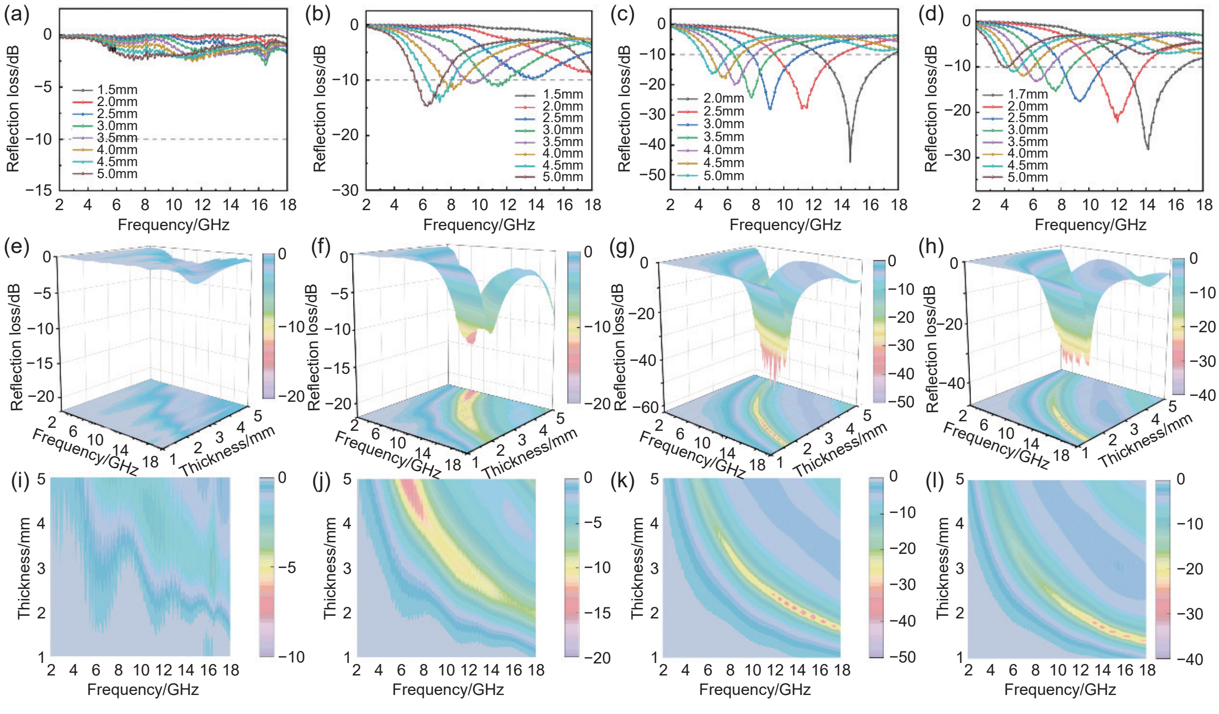

Fig. 6 (a–d) 2D RL diagrams. (e–h) 3D RL diagrams. (i–l) corresponding top views of CFC, CFC-1, CFC-2 and CFC-3

sistent with the $RL_{\min}$ matching thickness in the 2D diagrams, corresponding to the optimal absorption positions.

The ε' versus ε'' curve exhibits a Cole–Cole semicircle. To further investigate the dielectric loss mechanism of the material, Cole–Cole semicircles were plotted for the 4 samples. According to the Debye theory, each semicircle corresponds to a Debye relaxation process, whereas the elongated tail denotes conductive loss. The Debye relaxation can be described by Eq. (8)[43–44].

$$\left(\varepsilon' - \frac{\varepsilon_s+\varepsilon_\infty}{2}\right)+\left(\varepsilon''\right)^2=\left(\frac{\varepsilon_s-\varepsilon_\infty}{2}\right)^2 \tag{8}$$

where ε_s represents the static dielectric constant and ε_∞ denotes the relative dielectric constant at infinite frequency. Fig. 8(a–d) show the Cole–Cole semicircle curves of CFC, CFC-1, CFC-2 and CFC-3. Multiple Cole–Cole semicircles in CFC indicate the occurrence of various polarization relaxation processes, whereas the upward tail represents conductive loss. Compared with CFC, the three samples containing PPy exhibit extended tail lines, suggesting that PPy addition markedly enhances conductive loss and improves the loss performance of the material.

The EMW absorption performance is influenced by dielectric loss and substantially by magnetic loss. Within the test frequency range of 2–18 GHz, magnetic loss primarily arises from natural resonance, exchange resonance, and eddy current loss. The C_0 value, calculated using Eq. (9), evaluates the contribution of eddy current loss. The constant C_0 indicates

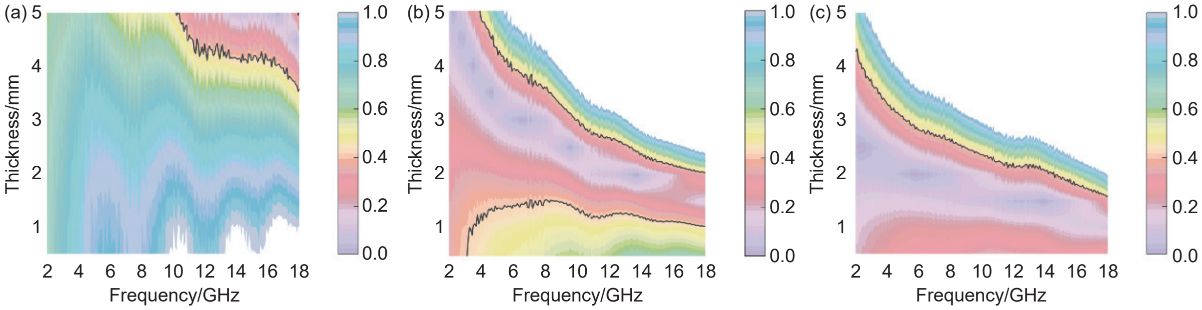

Fig. 7 Impedance matching |Δ| of CFC-1, CFC-2 and CFC-3

that magnetic loss is predominantly attributable to eddy current loss[45]. Fig. 8e presents the C_0 curves for the 4 samples. Within 2–6 GHz, the C_0 values for all samples decrease with increasing frequency, indicating the presence of natural resonance. Within 6–16 GHz, C_0 remains relatively stable, suggesting that eddy current loss is predominant. The 16–18 GHz range corresponds to exchange resonance. Overall, eddy current losses dominate the magnetic loss across the entire test frequency band[25].

$$C_0 = \mu''\left(\mu'\right)^{-2} f^{-1} \tag{9}$$

The attenuation constant is a key parameter for assessing the wave-absorbing performance of EMW-absorbing materials. It quantifies the material ability to dissipate EMW and is calculated using Eq. (10)[46–47].

$$\alpha = \frac{\sqrt{2}\pi f}{c} \times \sqrt{(\mu''\varepsilon'' - \mu'\varepsilon') + \sqrt{(\mu''\varepsilon'' - \mu'\varepsilon')^2 + (\mu'\varepsilon'' - \mu''\varepsilon')^2}} \tag{10}$$

Fig. 8f shows the relationship between attenuation constants and frequency for the 4 samples. The attenuation constants of all samples increase with rising frequency. CFC exhibits the lowest attenuation constant and the poorest impedance matching, indicating the least effective EMW absorption. However, CFC-2 and CFC-3 demonstrate larger attenuation constants and improved impedance matching, suggesting superior EMW absorption performance.

To further investigate the relationship among *RL*, thickness and impedance matching, specific thicknesses were changed for CFC-2 and CFC-3, and the curves of *RL*, quarter-wavelength, and impedance matching were plotted. As the thickness increases, the absorption peak shifts toward lower frequencies, consistent with the quarter-wavelength theory. The quarter wavelength can be expressed using Eq. (11)[48–49].

$$t_m = \frac{nc}{4f\sqrt{|\mu_r||\varepsilon_r|}} (n = 1, 3, 5\cdots) \tag{11}$$

When the frequency and matching thickness satisfy this equation, the incident EMW undergoes a 180° phase shift upon reflection, producing an interference that attenuates its energy. Fig. 9(a, b) display the 2D *RL* diagrams for CFC-2 and CFC-3 at specific thicknesses. In Fig. 9(c, d), black lines represent calculated results on the basis of the quarter-wavelength theory, whereas red dots denote experimentally measured data. The close correspondence between the two indicates that CFC-2 and CFC-3 follow the quarter-wavelength theory. The $|Z_{in}/Z_0|$ represents the degree of impedance matching, with values closer to 1, indic-

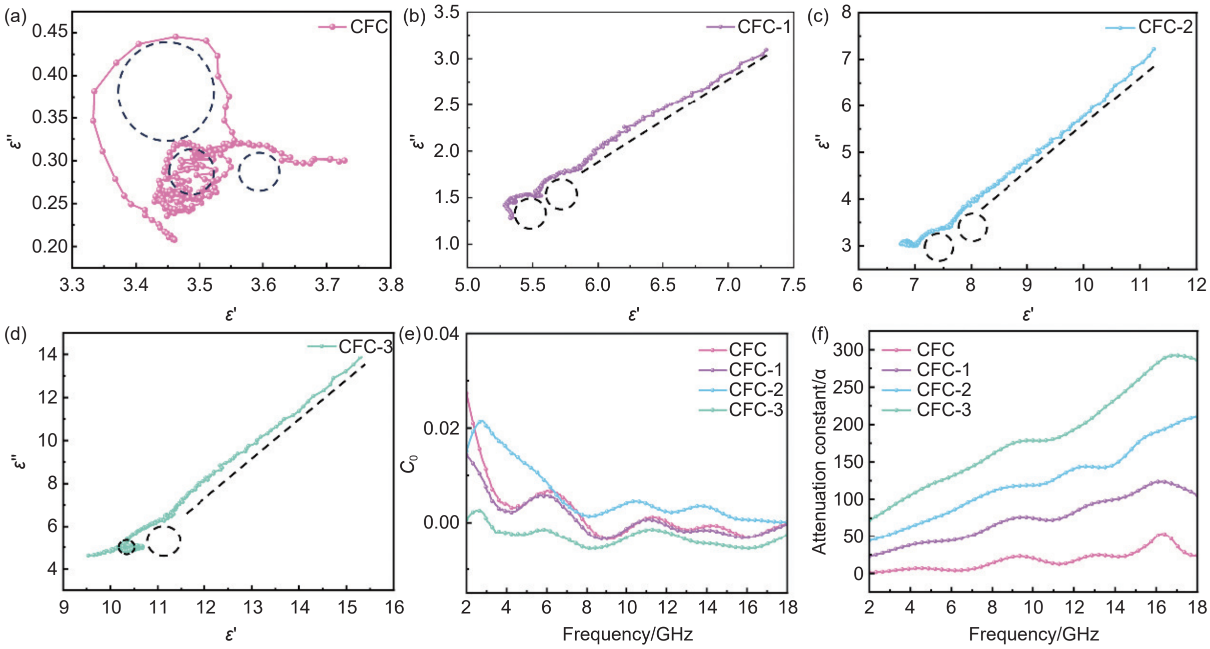

Fig. 8 (a–d) Cole–Cole semicircle curves, (e) C_0 curves and (f) attenuation constants of CFC, CFC-1, CFC-2 and CFC-3 ating better impedance matching. Fig. 9(e, f) illustrate the impedance matching diagrams for CFC-2 and CFC-3 at specific thicknesses, demonstrating good alignment with the quarter-wavelength theory. Notably, CFC-2 at a thickness of 2.0 mm satisfies the quarter-wavelength condition and achieves an impedance matching of 1, thereby attaining optimal absorption performance. Thus, optimal absorption performance occurs when the quarter-wavelength condition is met and impedance matching reaches 1.

To investigate EMW absorption performance under real application conditions, a CST-based simulation model was established to analyze the stealth performance of the materials using RCS analysis. The 3D EMW scattering signals of the original perfect electric conductor (PEC) and CoFe/C@PPy-coated plates were simulated at 14.64 GHz using a plane wave as the excitation source. Open boundary conditions were applied in all directions. The simulation model incorporated a 2-mm-thick absorption layer and a 0.5-mm-

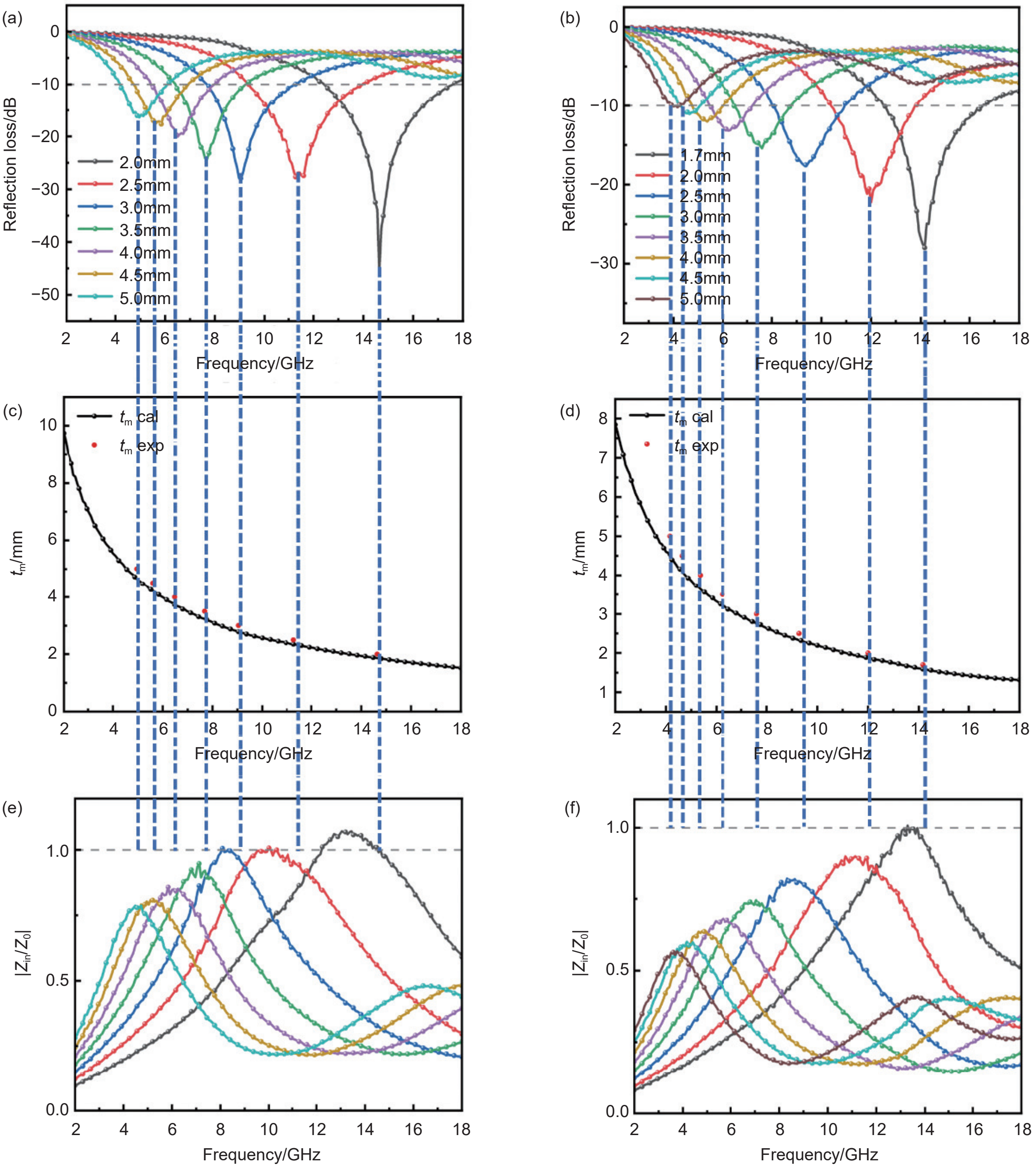

Fig. 9 (a, b) 2D RL. (c, d) Quarter-wavelength matching and (e, f) impedance matching of CFC-2 and CFC-3 at different thicknesses thick PEC layer, configured as a square with a side length of 150 mm. The positive Z-axis was selected as the incident direction, and the polarization direction was aligned along the X-axis. Fig. 10(a–d) present the 3D intensity images of the *RL* signals for CFC, CFC-1, CFC-2 and CFC-3 covering the PEC. All four samples display a small appearance area, indicating their stealth capability. Notably, CFC-2 demonstrates the smallest frontal area, reflecting its enhanced stealth capability. Fig. 10e shows the RCS simulation curves of PEC and the 4 samples across −90°-90°. All four samples exhibit lower RCS values than PEC, confirming their stealth effects. Importantly, the RCS values of CFC-2 remain predominantly below −20 dBm^2. Fig. 10f illustrates the RCS reduction values of the 4 samples at specific angles. Evidently, at 0°, 30° and 60°, CFC-2 shows markedly the highest RCS reduction among all samples. In particular, at 0°, the maximum RCS reduction reaches 37.5 dBm^2, indicating that the CFC-2 coating effectively attenuates EMW. The CST simulation results are highly consistent with the experimental findings, demonstrating that CFC-2 is a viable candidate for EMW absorption applications.

Based on the preceding analysis, Fig. 11 illustrates the potential microwave absorption mechanism of the CFC-2 composite. (1) The fiber structure extends the EMW transmission path within the material, enabling effective attenuation through multiple reflections and scattering. (2) The PPy coating forms a 3D conductive network on the fiber surface, facilitating electron migration and hopping under the alternating electric field, thereby enhancing conductive loss. (3) The fibers are rich in N atoms. N, as an efficient dipole polarization center, considerably enhances the polarization loss capacity under alternating electric fields by introducing intrinsic and defect dipole moments. (4) The structure contains numerous heterogeneous interfaces that contribute to interfacial polarization. (5) Magnetic metals, such as Fe and Co, introduce magnetic losses, including natural resonance, exchange resonance and eddy current loss. (6) Favorable impedance matching arising from complex permittivity and permeability enables EMW to penetrate the material without reflection. By integrating conductive loss, magnetic loss, and impedance matching, the CFC-2 composite exhibits outstanding EMW absorption performance.

Table 1 presents the recently reported comparable absorbers. In comparison, the CFC-2 composite in this study has a lower filling rate and reduced thickness, demonstrating that it is an efficient, lightweight

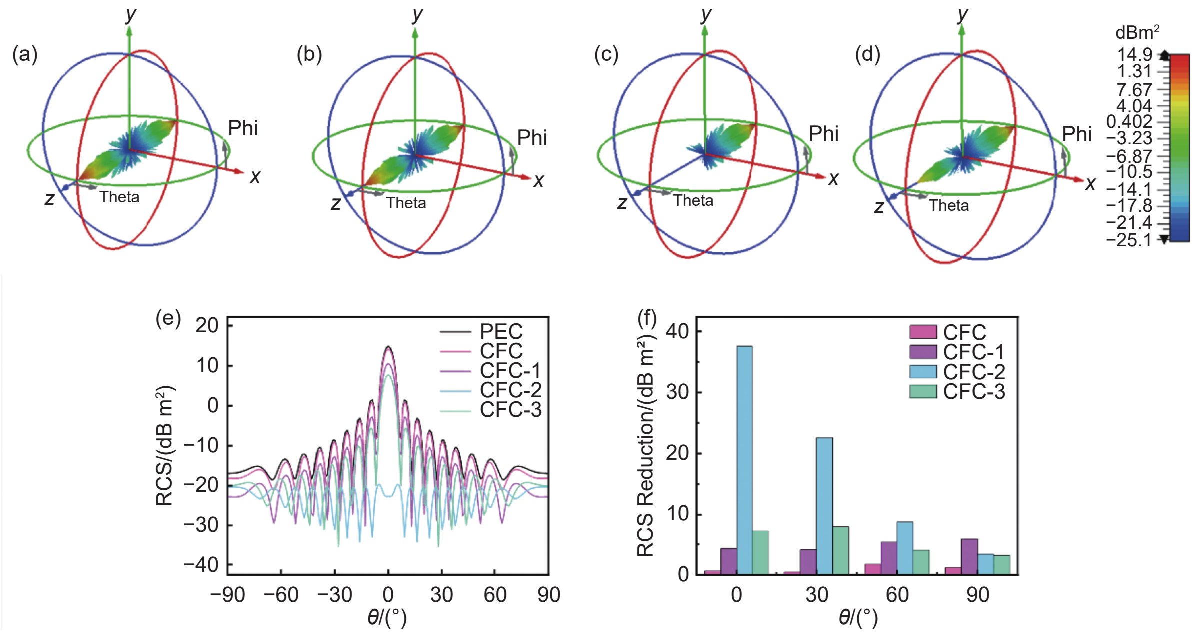

Fig. 10 (a–d) 3D RCS simulation results of CFC, CFC-1, CFC-2, and CFC-3. (e) RCS simulation curves and (f) bar chart of RCS reduction values at specific angles

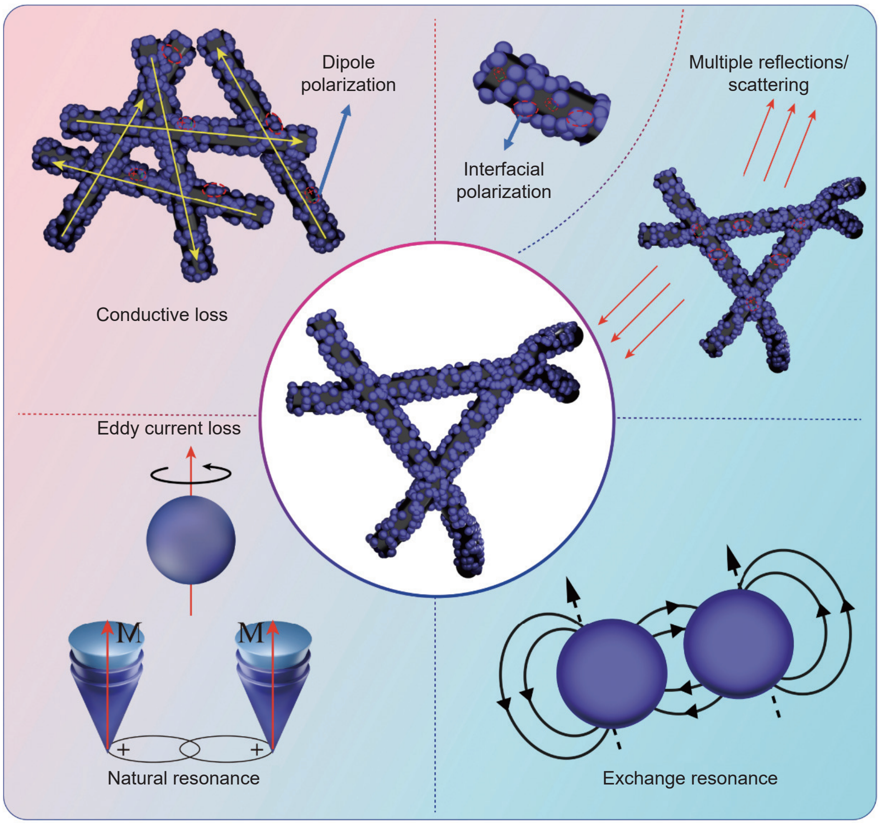

Fig. 11 EMW absorption mechanism of CFC-2

Table 1 Comparison of microwave absorbing properties of the material in this study with other materials in recent years

Sample	Loading/%	RL_{min}/dB	Thickness/mm	EAB/GHz	Thickness/mm	Ref.
Fe_3O_4/C	40	−57.1	5.1	4.0	5.1	[50]
C/FeCo/Fe	50	−52.2	2.9	6.7	2.4	[51]
CNOs@PANI	20	−47.8	1.5	4.4	1.5	[52]
Fe/Fe_3O_4/C	30	−40.1	5.5	3.3	5.5	[53]
Mxene/PPy/Fe_3O_4	35	−55.2	3.3	3.4	1.4	[54]
Co/NC@PANI	30	−46.3	5.0	3.5	2.5	[55]
CoFe/C@PPy	10	−45.6	2.0	5.1	2.0	This study

EMW-absorbing material.

4 Conclusion

This study synthesized CoFe/C@PPy composites using electrospinning, high-temperature calcination, and oxidative polymerization. By controlling the PPy content, the electromagnetic parameters were effectively regulated, resulting in enhanced EMW absorption performance. The optimally-prepared CFC-2 exhibits excellent wave-absorbing properties, achieving an RL_{min} of −45.6 dB at 14.64 GHz with the thickness of 2.0 mm, a filling rate of only 10%, and an *EAB* of 5.12 GHz. The strong absorption performance can be attributed to dielectric and magnetic losses, a unique structure, and effective impedance matching. Moreover, the absorption performance under real application scenarios was simulated using CST. Compared with the pure PEC board, the CFC-2-coated PEC layer exhibits an RCS consistently below −20 dBm^2 over the angular range of −90° to 90°. Notably, at $\theta = 0°$, it achieves an RCS reduction of 37.5 dBm^2, demonstrating its excellent EMW absorption capability in real applications. This study lays the foundation for developing electromagnetic functional materials with broad application potentials.

Declaration of competing interest

The authors declare that they have no known competing financial interests or personal relationships that could have appeared to influence the work reported in this paper.

Acknowledgements

This research was supported by the National Natural Science Foundation of China (52371231), Key R&D Program of Shanxi Province (202302040201008), and Natural Science Foundation of Shanxi Province (202203021212205).

References

[1] Zheng F, Wu P, Wang L, et al. Activated graphite with richly oxygenated surface from spent lithium-ion batteries for microwave absorption[J]. Small, 2025, 21: 2409454.

[2] Wu P, Kong X, Feng Y, et al. Phase Engineering on amorphous/crystalline γ-Fe_2O_3 nanosheets for boosting dielectric loss and high-performance microwave absorption[J]. Advanced Functional Materials, 2024, 34: 2311983.

[3] Kong X, Wu P, Tian S, et al. All-in-one: Multi-parameter engineering on γ-Fe_2O_3 for ultra-broadband microwave absorption [J]. Chemical Engineering Journal, 2024, 485: 150144.

[4] Liu P, Cui Z, Sun Y, et al. Research on high-entropy spinel microwave absorption materials: Exploration of machine learning and experimental integration[J]. Ceramics International, 2024, 50(23): 49906-49914.

[5] Huo Y, Wang Z, Zhang Y, et al. High-entropy ferrite with tunable magnetic properties for excellent microwave absorption[J]. International Journal of Minerals, Metallurgy and Materials, 2025, 32(3): 668-677.

[6] Wu D dan, Zhang H xiao, Wang Z yan, et al. 3D porous $NiCo_2(CO_3)_3$/reduced graphene oxide aerogel with heterogeneous interfaces for high-efficiency microwave absorption[J]. New Carbon Materials, 2023, 38(6): 1035-1049.

[7] Lv Y, Tian J, Chen Z, et al. MXene/bimetallic CoNi-MOF derived magnetic-dielectric balanced composites with multiple heterogeneous interfaces for excellent microwave absorption[J]. Chemical Engineering Journal, 2023, 478: 147413.

[8] Sumanta S, Rajesh K, Sung S H. Low-value biomass-derived carbon composites for electromagnetic wave absorption and shielding: A review[J]. New Carbon Materials, 2025, 40(2): 293-316.

[9] Chen G, Zhang L, Fan X, et al. Interfacial and defect polarization in MXene-like laminated spinel for electromagnetic wave absorption application[J]. Journal of Colloid and Interface Science, 2021, 588: 813-825.

[10] Mandal D, Bhandari B, Mullurkara S V, et al. All-around electromagnetic wave absorber based on Ni–Zn ferrite[J]. ACS Applied Materials & Interfaces, 2024, 16: 33846-33854.

[11] Jiabin Ma, Biao Zhao, Huimin Xiang, et al. High-entropy spinel ferrites MFe_2O_4 (M = Mg, Mn, Fe, Co, Ni, Cu, Zn) with tunable electromagnetic properties and strong microwave absorption[J]. Journal of Advanced Ceramics, 2022, 11(5): 754-768

[12] Xia Y, Gao W, Gao C. A Review on graphene-based electromagnetic functional materials: electromagnetic wave shielding and absorption[J]. Advanced Functional Materials, 2022, 32: 2204591

[13] Li Z, Liang J, Wei Z, et al. Lightweight foam-like nitrogen-doped carbon nanotube complex achieving highly efficient electromagnetic wave absorption[J]. Journal of Materials Science & Technology, 2024, 168: 114-123.

[14] Chen J, Zheng J, Huang Q, et al. Carbon fibers@Co-ZIFs derivations composites as highly efficient electromagnetic wave absorbers[J]. Journal of Materials Science & Technology, 2021, 94: 239-246.

[15] Luo J, Lv Z, Zhang L, et al. Modulation of dielectric behavior in ceramic-based materials for integrated electromagnetic waves absorption and thermal conduction[J]. Advanced Functional Materials, 2025, 35: 2420086

[16] Yan J, Huang Y, Liu X, et al. Polypyrrole-based composite materials for electromagnetic wave absorption[J]. Polymer Reviews, 2021.

[17] Dai B, Li J, Liu X, et al. Multiple synergistic losses in the absorption of electromagnetic waves by three-dimensional cross-linked carbon fiber[J]. Carbon, 2022, 195: 308-318.

[18] Xie K, Zhang Q, Chen F, et al. Largely enhanced electromagnetic wave absorption via surface coating of carbonyl iron particles with liquid metal[J]. Journal of Materials Chemistry A, 2025, 13: 1887-1896.

[19] Kong L, Cui H, Zhang S, et al. Absorption frequency band switchable intelligent electromagnetic wave absorbing carbon composite by cobalt confined catalysis[J]. Journal of Materials Science & Technology, 2025, 211: 203-211.

[20] Chen L, Pan J, Wang T, et al. 1D magnetic nickel-carbon matrix nanotube composites derived from hydrogen-bonded organic frameworks and metal–organic frameworks for electromagnetic wave absorption[J]. Advanced Functional Materials, 2025, 35: 2409432.

[21] Guo Z, Zhang X, Lv C, et al. Advantageous synergistic strategy to construct Ni@C/PC composites for efficient electromagnetic wave absorption[J]. Carbon, 2025, 234: 120010.

[22] Tang Y, Ruan J, Xin Y, et al. Organic acid etching strategy for synthesis of ZIF-8@ZIF-67-derived hollow Co@C/C rods with excellent electromagnetic wave absorption in C-band[J]. Chemical Engineering Journal, 2025, 511: 161999.

[23] Han H, Lou Z, Wang Q, et al. Introducing rich heterojunction surfaces to enhance the high-frequency electromagnetic attenuation response of flexible fiber-based wearable absorbers[J]. Advanced Fiber Materials, 2024, 6: 739-757.

[24] Wang Y, Xian G, Wu C, et al. Broadband electromagnetic wave absorption of Fe@polyaniline-derived carbon composites with nitrogen-doping[J]. Diamond and Related Materials, 2022, 130: 109472.

[25] Dai B, Dong F, Wang H, et al. Fabrication of CuS/Fe_3O_4@polypyrrole flower-like composites for excellent electromagnetic wave absorption[J]. Journal of Colloid and Interface Science, 2023, 634: 481-494.

[26] Feng S, Wang H, Ma J, et al. Fabrication of hollow Ni/NiO/C/MnO_2@polypyrrole core-shell structures for high-performance electromagnetic wave absorption[J]. Composites Part B: Engineering, 2024, 275: 111344.

[27] Liao Z, Ma M, Tong Z, et al. Fabrication of $ZnFe_2O_4$/C@PPy composites with efficient electromagnetic wave absorption properties[J]. Journal of Colloid and Interface Science, 2021, 602: 602-611.

[28] Liu D, Qiang R, Du Y, et al. Prussian blue analogues derived magnetic FeCo alloy/carbon composites with tunable chemical composition and enhanced microwave absorption[J]. Journal of Colloid and Interface Science, 2018, 514: 10-20.

[29] Ma M, Liao Z, Su X, et al. Magnetic CoNi alloy particles embedded N-doped carbon fibers with polypyrrole for excellent electromagnetic wave absorption[J]. Journal of Colloid and Interface Science, 2022, 608: 2203-2212.

[30] Olad A, Shakoori S. Electromagnetic interference attenuation and shielding effect of quaternary Epoxy-PPy/Fe_3O_4-ZnO nanocomposite as a broad band microwave-absorber[J]. Journal of Magnetism and Magnetic Materials, 2018, 8458: 335–345.

[31] Bi Y, Ma M, Liao Z, et al. One-dimensional Ni@Co/C@PPy composites for superior electromagnetic wave absorption[J]. Journal of Colloid and Interface Science, 2022, 605: 483-492.

[32] Wei S, Shi Z, Li X, et al. Bimetallic MOF-derived CoFe@nitrogen-doped carbon composites for wide bandwidth and excellent microwave absorption[J]. Journal of Alloys and Compounds, 2022, 910: 164861.

[33] Pan Y, Cheng L, Lan D, et al. Conductor-semiconductor heterointerface polarization enhancement for superior electromagnetic wave absorption[J]. Journal of Materials Science & Technology, 2026, 244: 129-141.

[34] Zeng X, Cheng X, Yu R, et al. Electromagnetic microwave absorption theory and recent achievements in microwave absorbers[J]. Carbon, 2020, 168: 606-623.

[35] Wang Z, Jia Z, Ren J, et al. Multi-topological network engineering of Co/MnO composites for electromagnetic wave absorption[J]. Journal of Materials Science & Technology, 2025, 235: 81-90.

[36] Xu S, Jia Z, Lan D, et al. Synergistic polarization relaxation in heteroatom-optimized heterointerfaces for electromagnetic wave absorption[J]. Advanced Functional Materials, 2025, 35: 2500304.

[37] Feng S, Zhang H, Wang H, et al. Fabrication of cobalt-zinc bimetallic oxides@polypyrrole composites for high-performance electromagnetic wave absorption[J]. Journal of Colloid and Interface Science, 2025, 652: 1631-1644.

[38] Chen Q, Wang Y, Xiong Y, et al. Fiber materials for applications of electromagnetic wave absorption[J]. Advanced Fiber Materials, 2025, 7: 1320-1349.

[39] Mo P, Shui A, Yu H, et al. Facile synthesis of MoO_2/S-doped carbon nanofibers for ultra-high electromagnetic wave absorption[J]. Carbon, 2025, 237: 120121.

[40] Wei Z, Li Z, Chen D, et al. Recent Progress of Advanced Composites for Broadband Electromagnetic Wave Absorption[J]. Small Structures, 2025, 6: 2400615

[41] Zhao R, Liang B, Shi Y, et al. Recent progress of carbon-based magnetic fibers for electromagnetic wave absorption[J]. Carbon, 2024, 229: 119513.

[42] Dai B, Ma Y, Feng S, et al. Fabrication of one-dimensional M (Co, Ni) @polyaniline nanochains with adjustable thickness for excellent microwave absorption properties[J]. Journal of Colloid and Interface Science, 2022, 627: 113-125.

[43] Zhang Y, Liu X, Guo Z, et al. MXene@Co hollow spheres structure boosts interfacial polarization for broadband electromagnetic wave absorption[J]. Journal of Materials Science & Technology, 2024, 176: 167-175.

[44] Liu C, Han M, Lin J, et al. Wood biomass-derived carbon for high-performance electromagnetic wave absorbing and shielding[J]. Carbon, 2023, 208: 255-276.

[45] Wei M, Liu K, Wang Y, et al. Hierarchical magnetic carbon nanoflowers for ultra-efficient electromagnetic wave absorption[J]. Small, 2024, 20: 2402632.

[46] Liang S, Guan H, Zhang H, et al. Intelligent Off/On switchable electromagnetic wave absorbing material based on VO_2 nanowires[J]. Chemical Engineering Journal, 2024, 489: 151025.

[47] Zhu L, Wu W, Chen J, et al. High-performance electromagnetic wave absorption by two-dimensional mesoporous monolayer $Ti_3C_2T_x$ MXene[J]. Chemical Engineering Journal, 2024, 488: 150649.

[48] Li X, Luo J, Wang Q, et al. Synchronously formed hetero- and hollow core-branch nanostructure toward wideband electromagnetic wave absorption[J]. Small, 2024, 20: 2404609.

[49] Xie R, Chen Z, Ma W, et al. Utilization of waste biomass to produce SiO_2/SiC nanowires with efficient electromagnetic wave absorption performance[J]. Chemical Engineering Journal, 2024, 501: 157699.

[50] Wu X, Dong A, Xu S, et al. Efficient broadband sea urchin-like Fe_3O_4@C electromagnetic wave absorbing materials[J]. Journal of Magnetism and Magnetic Materials, 2024, 600: 172124.

[51] Wu L, Jin Y, Meng F, et al. Electromagnetic wave absorption composites C/Fe/CoFe by one-step method[J]. Solid State Communications, 2025, 397: 115815.

[52] Li S, Zhang L, Zhang X, et al. One-step synthesis of chestnut-like magnetic CNOs@PANI with microwedge enhanced electromagnetic wave absorption[J]. ACS Applied Electronic Materials, 2024, 6: 4608-4618.

[53] Yuan S, Wang T, Feng T, et al. Electromagnetic wave absorption of fabricated Fe/Fe_3O_4/C hollow fibers derived from ceiba fiber templates[J]. Materials Science and Engineering: B, 2024, 299: 117057.

[54] Zhang W, Xu H, Li Y, et al. Controllable synthesis of 3D porous MXene/polypyrrole/Fe_3O_4 with magnetically tunable pore structures for electromagnetic wave absorption[J]. Materials Chemistry and Physics, 2025, 336: 130507.

[55] Li R, Zhai F, Liu Y, et al. MOFs self-templated hollow Co/NC@PANI composites for high-efficiency electromagnetic absorption[J]. Synthetic Metals, 2024, 301: 117514.